A novel NIR-II FL/ PA imaging-guided synergistic photothermal-immune therapy: Biomineralizing nanosystems integrated with anti-tumor and bone repair

Xin Zhang [b,1], Dongsheng Li [c,1], Wenxuan Wang [b,1], Xiaochun Zheng [a,1], Chongqing Zhang [d,1], Yarong Jin [a], Shichao Meng [b], Jinxuan Li [b], Rong Dai [a], Weiwei Kang [a], Hua Wu [b,***], Ziliang Zheng [b,*], Ruiping Zhang [a,**]

[a] *Department of Radiology, Fifth Hospital of Shanxi Medical University (Shanxi Provincial People's Hospital), Taiyuan, 030000, China*
[b] *Department of Orthopedics, Third Hospital of Shanxi Medical University, Shanxi Bethune Hospital, Shanxi Academy of Medical Sciences, Tongji Shanxi Hospital, Taiyuan, 030032, China*
[c] *Research Team of Molecular Medicine, First Hospital of Shanxi Medical University, Shanxi Medical University, Taiyuan, 030001, China*
[d] *Medical Imaging Department, Shanxi Province Cancer Hospital (Shanxi Hospital Affiliated to Cancer Hospital, Chinese Academy of Medical Sciences/Cancer Hospital Affiliated to Shanxi Medical University), Taiyuan, 030001, China*

ARTICLE INFO

ABSTRACT

Advanced stages of breast cancer are frequently complicated by bone metastases, which cause significant cancer-related bone destruction and mortality. However, the early precise theranostics of bone metastasis remains a formidable challenge in clinical practice. Herein, a novel all-in-one nanotheranostic system (ABI NYs) combining NIR-II FL/PA dual-modal imaging with photothermal-immunity therapeutic functionalities in one component was designed to precisely localize bone metastasis microscopic lesions and achieve complete tumor ablation at an early stage. The surface modification of the nanosystem with ibandronate (IBN) facilitates both passive and active targeting, significantly improving the detection rate of bone metastasis and suppressing the bone resorption. Superior photothermal performance produces sufficient heat to kill tumor cells while stimulating the upregulation of heat shock proteins 70 (HSP70), which triggers the immunogenic cell death (ICD) effect and the anti-tumor immune response. These all-in-one nanosystems precisely demonstrated early lesion localization in bone metastases and total tumor ablation with a single integration via "one-component, multi-functions" technique. To sum up, ABI NYs, as novel biomineralizing nanosystems integrated with anti-tumor and bone repair, present a synergistic therapy strategy, providing insight into the theranostics of bone metastases and clinical research.

1. Introduction

Bone metastasis is a frequent complication of breast cancer that affects the quality of life and survival rate of patients severely. Approximately 80% advanced breast cancer patients developed incurable bone metastasis [1–3]. However, early-stage diagnosis of bone metastasis is challenging. Current diagnosis techniques, including digital radiography (DR), computed tomography (CT), magnetic resonance imaging (MRI), are limited in their ability to detect micrometastatic lesions [4]. Once patients were diagnosed with bone metastases, irreversible bone destruction has already occurred. More hopelessly, it is difficult to completely eliminate them by traditional therapies, such as localized radiation therapy or surgical resection [5,6]. Thus, the development of novel diagnostic and therapeutic strategies for bone metastasis is urgently needed to meet the clinical demands of bone metastasis and improve the prognosis of patients. Phototheranostics, a novel modality

that combines various diagnosis and therapy techniques, holds great promise for individualized precision healthcare owing to its biosafety, high spatial-temporal resolution, and non-invasiveness [7–9]. Integrating multiple diagnostics and therapeutic functions into a single nanosystem has the potential to provide real-time therapeutic effects monitoring and functional information, which is expected to provide value in guiding the precision treatment of bone metastases at early stage.

Currently, optical imaging has evolved into a new diagnostic approach for both clinical and basic biological research. It should be noted that optical imaging exhibits remarkable sensitivity and spatio-temporal resolution, and among them, fluorescent probes enable the specific visualization of subtle pathological changes owing to their improved signal-to-noise ratio [10,11]. The advent of fluorescence imaging in the second near-infrared window (NIR-II FL, 1000–1700 nm) is one of the most significant advancements for bone metastasis, which endows unparalleled tissue penetration and temporal-spatial resolution as well as negligible background interference than NIR I fluorescence imaging (700–900 nm) [12,13]. However, due to limitations of sensitivity and detection specificity, a single imaging detection technique is difficult to obtain the complete information of small tumor lesions. In particular, photoacoustic imaging (PAI) provides micrometer-scale resolution and penetration depth down to the centimeter, which is a significant addition to NIR-II FL imaging [14]. For example, Zhang et al. devised a bright NIR-II FL/PA probe to enable simultaneous and dynamic imaging of vasculatures and deep tissues [15]. Fan and co-workers reported a small-molecule dye combines the NIR-II FL/PA imaging for accurate deep tumor location and theranostics [16]. NIR-II FL/PA multi-modality imaging can offer both structural and function-related data in real time, which might be extremely beneficial in early guidance of precision bone metastases theranostic. Also, besides serving as excitation of optical imaging, light can trigger phototherapies, emerged with excellent spatial specificity and non-invasiveness compared with traditional chemotherapies and radiotherapies [17].

Based on the multi-modality advantages imaging, the establishment of multifunctional synergy therapy nanosystems has emerged as a promising strategy for precision therapy. Photothermal therapy (PTT) has emerged as one of the most promising therapeutic techniques due to its high efficiency and minimal invasiveness [18,19]. PTT could induce tumor cell apoptosis by thermal ablation under NIR irradiation and the secondary immunity response [20–22]. Heat shock proteins 70 (HSP70) is an important immune modulator, and is now appreciated to play a role as an extracellular signaling molecule, furthermore stated to possess the capacity to effectively transport antigens to dendritic cells (DCs) [23, 24]. Research by Moehler et al. Arnold et al., and Cao et al. shown that HSP70, which is produced by dead tumor cells, can enhance the presentation of tumor antigens and function as a potent adjuvant to stimulate protection against cancer [25]. More recently, Li et al. proved that photothermal performance under NIR light irradiation induce the upregulation of HSP70, further enhance the infiltration of activated T cells into tumors, which resulted in superior tumor inhibition efficacy [26]. Nonetheless, numerous photosensitizers are limited by poor targeting and insufficient tumor enrichment to achieve efficient imaging-guided photothermal therapy and the integration of anti-tumor and bone-repair. Hence, it is urgently needed to achieve early tumor suppression and bone repair under the premise of precise targeting.

Herein, an all-in-one nanotheranostic system (AgBiS$_x$@BSA-IBN, ABI NYs) is developedfor the early effective bone metastasis therapy under the guidance of NIR-II FL/PA bimodal imaging (Scheme 1). Firstly, AgBiS$_x$@BSA was successfully synthesized via a simple and environmentally friendly biomineralization technique. Remarkably, AgBiS$_x$@BSA can dramatically enhance the NIR-II FL performance by providing higher signal-to-background ratio and spatial resolution, thus allowing for precise early tumor localization. Secondly, AgBiS$_x$@BSA was conjugating with ibandronate (IBN), a third-generation bisphosphonate, which been employed as a bone-targeting agent and inhibition of osteolysis. ABI NYs are able to accurately localize microscopic lesions of early bone metastases and improve the detection rate through an active and passive dual-targeting strategy guided by NIR-II FL/PA dual-mode imaging. Thirdly, under NIR light irradiation, ABI NYs exhibits excellent photothermal performance by producing sufficient heat to kill tumor cells. Meanwhile, the upregulation of HSP70 is accompanied by the irradiation of NIR, further provoke the immunogenic cell death (ICD) effect and anti-tumor immune response. Taken
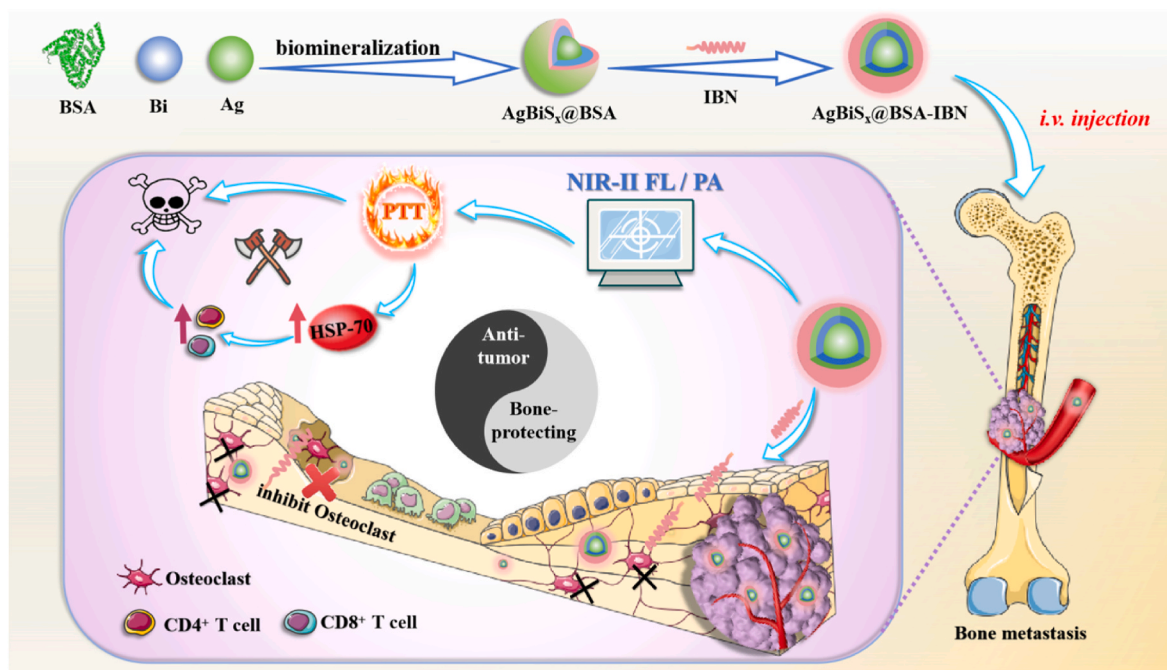
Scheme 1. Schematic depiction of ABI NYs preparation, and usage as all-in-one nanosystems for NIR-II FL/PA imaging-guided synergistic treatment of bone metastases.

together, the novel bone-targeting phototheranostic agent not only effectively inhibits tumor growth and early osteolysis, but also realizes NIR-II/PA bimodal imaging-guided PTT-ICD synergistic treatment, which will provide new insights into the development of nano-theranostic for bone metastasis.

2. Results and discussion

The AgBiS$_x$ nanoparticles modified with BSA were obtained through biomineralization, followed by successful conjugation of IBN to AgBiS$_x$@BSA. The synthesized nanoparticles exhibited a relatively homogeneous size distribution with an average diameter of approximately 6 nm (Fig. 1A), indicating the successful construction of ABI NYs. Moreover, the high-resolution transmission electron microscopy (HRTEM) image of the ABI NYs indicated two separate fringes with interplanar lengths of 0.25 nm and 0.33 nm (Fig. 1B). These values match to the lattice spacing measured in the (121) planes of monoclinic α-Ag$_2$S and (211) planes of monoclinic Bi$_2$S$_3$ [27,28]. The successful synthesis of ABI NYs was confirmed by elemental mapping using energy dispersive X-ray spectroscopy (EDS), which demonstrated the distribution of Ag and Bi (Fig. 1C). All of the anticipated elements are seen in the X-ray photoelectron spectroscopy (XPS) shown in Fig. S1, and the spectra thoroughly corroborated the successful construction of the ABI NYs. More specifically, the Ag XPS spectrum exhibited two distinct peaks at 367.4 and 373.5 eV, corresponding to the Ag 3d5/2 and 3d3/2 orbitals, respectively, providing strong evidence for the formation of Ag$_2$S (Fig. 1D) [29]. Furthermore, the XPS spectra displayed that the

peaks corresponding to Bi 4f7/2 and Bi 4f5/2 could be attributed to the presence of the Bi$_2$S$_3$ phase (Fig. 1E). Additionally, the X-ray diffraction pattern (XRD) proved the crystallization of ABI NYs in Fig. S2.

To determine the chemical structure of ABI NYs, Fourier-transform infrared (FT-IR) spectra analysis was carried out (Fig. 1F). The amide II bands, the –OH stretching vibration mode, and the C═O stretching vibration are responsible for the absorption bands at 1654 cm^{-1}, 1541 cm^{-1}, and 3437 cm^{-1} [30]. Meanwhile, the band at 1230 cm^{-1} corresponding to the asymmetric phosphate stretching of IBN also emerged in ABI NYs [31]. In addition, based on thermo-gravimetric analysis (TGA) of AB and ABI NYs (Fig. 1G), the observed weight discrepancy between two NYs can be related to the presence of IBN, exhibiting remarkable co-loading capacities up to 5.2 wt%. According to the results of dynamic light scattering (DLS), the diameter of ABI NYs was somewhat larger (15 ± 1.3 nm) compared to the TEM results, which could be attributed to the presence of hydrated layers (Fig. 1H). The zeta potential of ABI NYs was −45.1 ± 1.62 mV, which can be ascribed to the substantial negative surface charge exhibited by BSA. This characteristic plays a pivotal role in extending the duration of blood circulation. Remarkably, no discernible changes in size or zeta potential of ABI NYs were noticed even after 24 h incubation period, demonstrating the excellent stability of ABI NYs in various solutions (PBS, cell medium, and fetal bovine serum (FBS)) (Fig. S3). In consideration of the complex biological environment *in vivo*, the long-term stability of ABI NYs was tested. The DLS and PDI measurements further showed that ABI NYs retained their long-time stability in different solution after 7 days, indicating that the ABI NYs exhibited great physiological stability and prolonged blood
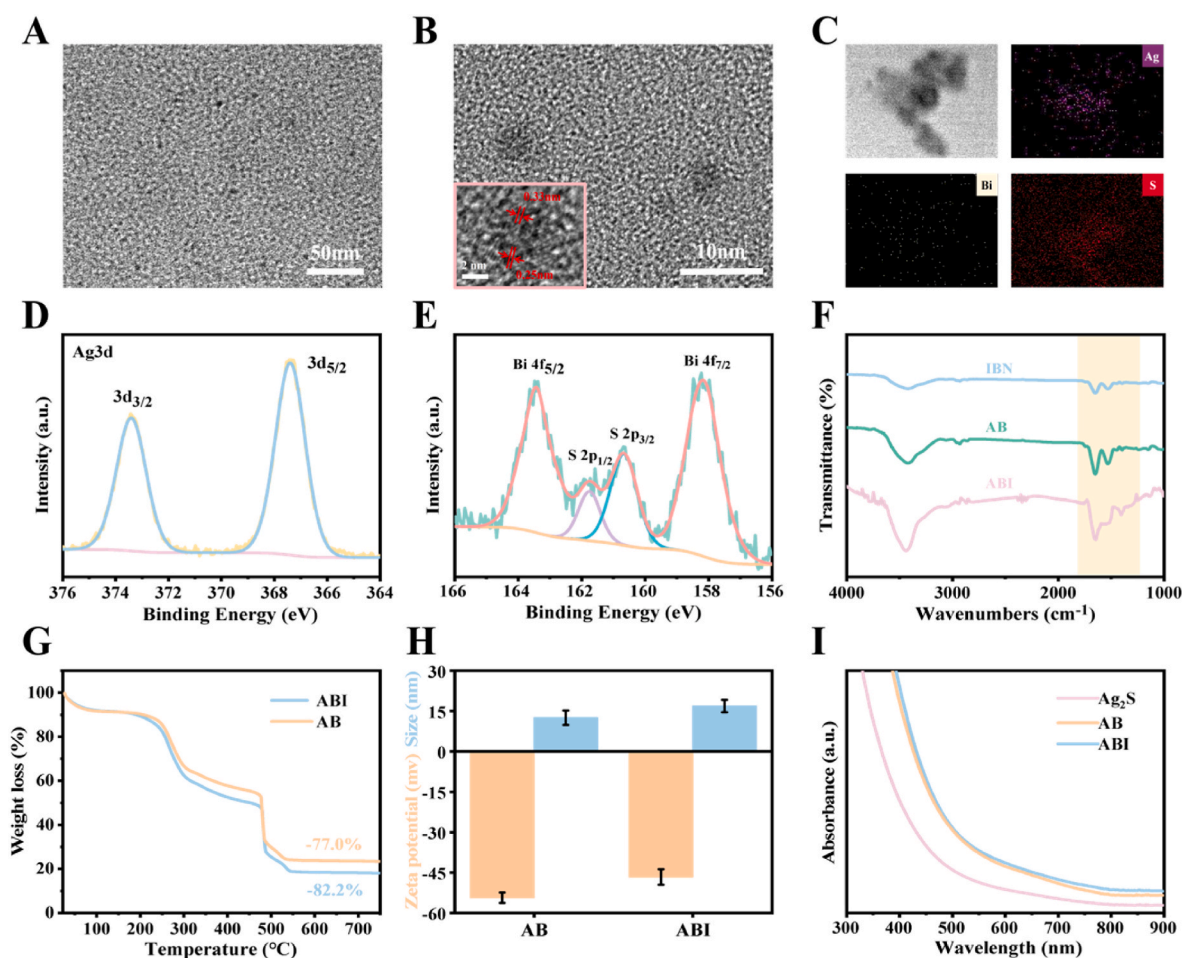

Fig. 1. A) Compositional and structural characterizations of ABI NYs. B) TEM images of ABI NYs. C) Corresponding elemental mappings of ABI NYs. XPS analysis of D) Ag 3d and E) Bi 4f spectra of ABI NYs. F) FTIR spectra of AB and ABI NYs. G) TG weight loss profiles of AB and ABI NYs, respectively. H) Hydrodynamic size and zeta potential of ABI NYs. I) UV–vis absorption spectra of Ag$_2$S, AB, and ABI NYs.

circulation (Fig. S4). We expected that ABI NYs would effectively accumulate at the site of bone metastases through enhanced permeability and retention (EPR) effects, as well as by leveraging the bone-targeting ability of IBN. The UV–vis absorption spectra of ABI NYs presented in Fig. 1E revealed a broad absorption band below 900 nm, demonstrating its ability to absorb NIR light and excellent performance in PA imaging and PTT (Fig. 1I).

Because of the broad absorption of ABI NYs in the NIR-II region, we decided to investigate systematically the photothermal performance of ABI NYs under laser irradiation (808 nm, 1 W/cm^2) for 5 min (Fig. 2A). The temperature increased at a pronounced concentration-dependent (0–800 μg/mL, 1.0 mL) rate. It should be mentioned that ABI NYs at 400 μg/mL may reach 50.2 °C in 5 min and ascend to 43.7 °C during a short 150-s irradiation interval. In stark contrast, the temperature of pure water remained unchanged under identical irradiation conditions (<5 °C). Furthermore, the photothermal stability of ABI NYs remain excellent even after five repeated on/off cycles while exposed to 808 nm laser (Fig. 2B). To further evaluate the NIR-II photothermal performance, the ABI NYs (400 μg/mL) were irradiated under 808 nm laser at elevated power densities (0.5, 0.75, 1.25, and 1.5 W/cm2). The temperature of the ABI NYs increased rapidly and reached a plateau within 5 min, with the rising rate positively correlated with the laser power (Fig. S6). Based on the available methodologies, the photothermal conversion efficiency (η) of the ABI NYs was calculated to be 35.6%

(Fig. S7) [32]. As depicted in Fig. 2C, the ABI NYs exhibited distinct PA signals, which was correlated linearly with increasing concentrations of ABI NYs within the concentration range of 0–800 μg/mL. Thus, ABI NYs have significant potential as an effective PA imaging therapeutic agent.

As shown in Fig. 2D, ABI NYs produced stronger NIR-II FL at around 1200 nm than Ag$_2$S, and exhibited a notable redshift. These indicated that the inclusion of Bi significantly enhanced the fluorescence intensity. Therefore, the optical properties of ABI NYs in the NIR-II window offer advantages in terms of enhanced imaging depth and reduced autofluorescence *in vivo* tissue, possessing the potential for NIR-II fluorescence imaging of bone metastases. In addition, the concentration of ABI NYs exhibited a linear correlation with its fluorescence intensity, thereby demonstrating its feasibility for signal quantification (Fig. 2E). The affinity of NYs for bone is a critical factor to target bone metastatic lesions. Next, the bone-specific affinity of ABI NYs was evaluated *in vitro*. A primary constituent of bone, hydroxyapatite (HA), was employed for *in vitro* osseointegration investigations. The HA was exposed to varying concentrations of ABI NYs for 3 h, resulting in the intensified FL intensity of the precipitated HA. In contrast, negligible fluorescence was observed in HA precipitates following incubation with various concentrations of AB without specific targeting of the IBN ligand (Fig. 2F). Incubating HA bone slices in the precence or absence of IBN further supported this result (Fig. 2G). Notably, ABI NYs exbited high specificity in binding to bone components, even under complex physiological
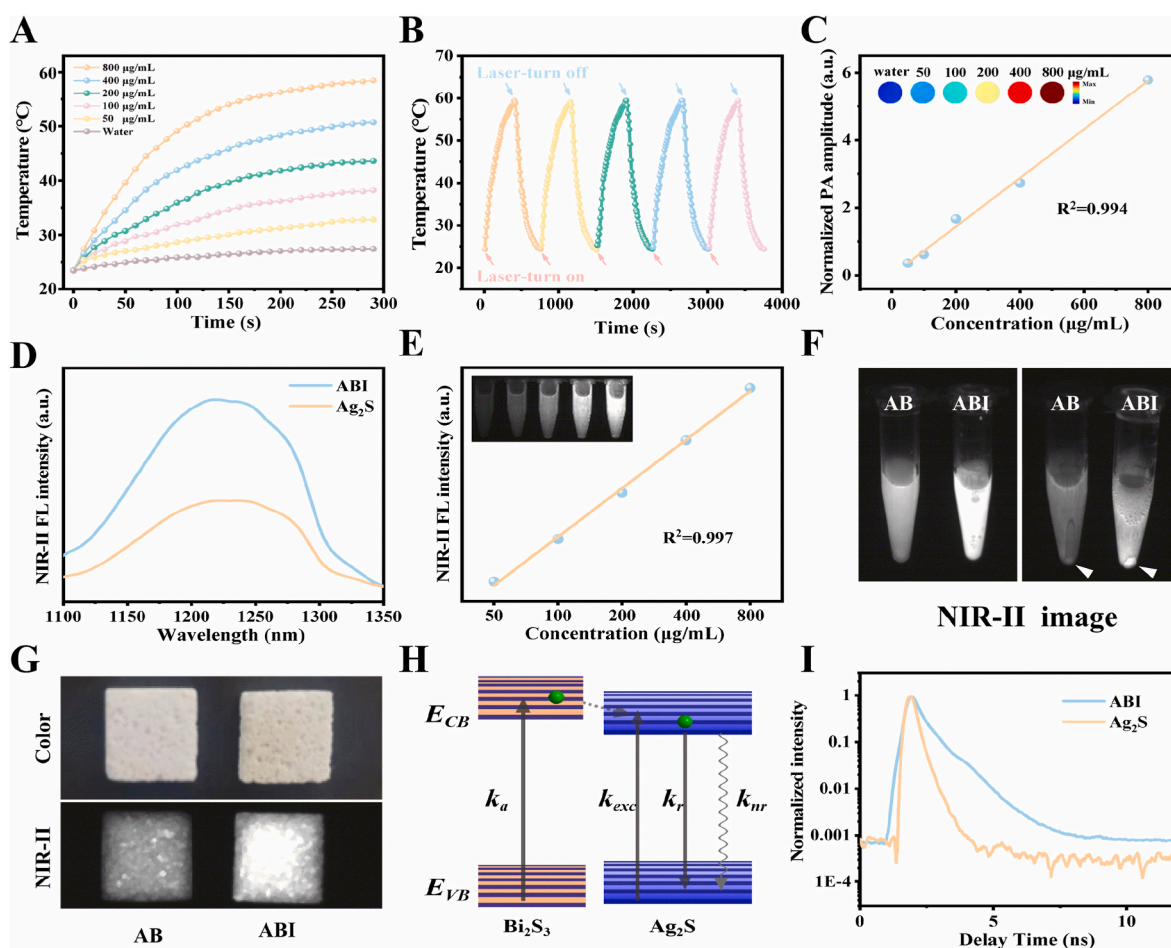

Fig. 2. A) Temperature changes of ABI NYs at different concentrations (0, 50, 100, 200, 400, and 800 μg/mL) 1 W/cm^2 under 808 nm laser irradiation (1 W/cm^2). B) The photothermal stability of ABI NYs for five on/off cycles (1.0 W/cm^2). C) PA signal intensity of ABI NYs as a function of concentrations ranging from 0 to 800 μg/mL, under 808 nm laser (0.3 W/cm^2) irradiation. D) Fluorescence spectra of Ag$_2$S and ABI NYs. E) NIR-II FL intensity and images at different concentrations of ABI NYs (50, 100, 200, 400, and 800 μg/mL). F) Hydroxyapatite-binding NIR-II fluorescence image of AB and ABI NYs. G) Representative NIR-II fluorescence images of bone slices were treated with AB, and ABI NYs. H) Schematic illustration of energy scheme for ABI NYs and their electron transfer. I) The fluorescence lifetime of Ag$_2$S and ABI NYs.

conditions which contain multiple biomolecules (Fig. S8).

ABI NYs has better light absorption than Ag_2S, which is reflected not only in superior PA imaging performance, but also in stronger fluorescence emission. As shown in Fig. 2D, ABI NYs has stronger fluorescence emission and some spectral changes, but the overall spectral shape is similar to the spectrum of Ag_2S. It can be seen that the fluorescence-emitting body of ABI NYs is still Ag_2S, and the doping of Bi contributes to a larger absorption cross-section and a slight change to the energy level structure of Ag_2S. As shown in Fig. 2H–a schematic diagram of the energy level structure of ABI NYs was constructed to demonstrate that the Bi_2S_3 formed after Bi is mixed, and after absorbing more energy, part of it contributes to photoacoustic imaging, and the other part is

transferred to Ag_2S to enhance fluorescence emission. The energy transfer process also increases the fluorescence lifetime of ABI NYs, as shown in Fig. 2I.

To effectively visualize the cellular uptake behavior, NIR-II FL was utilized to monitor the processes of phagocytosis as well as distribution in 4T1 cells (Fig. 3A). Following co-incubation with ABI NYs, there was a time-associated increase in fluorescence intensity, suggesting that ABI NYs had superior cellular absorption capacity. (Fig. 3B). As evidenced by its exceptional NIR-II fluorescence brightness, ABI NYs was confirmed as an outstanding NIR-II fluorescence probe. Then, the *in vitro* cytotoxicity of ABI NYs was evaluated in human umbilical vein endothelial cells (HUVEC) by cell counting kit8 (CCK8) assay (Fig. 3C). Remarkably,
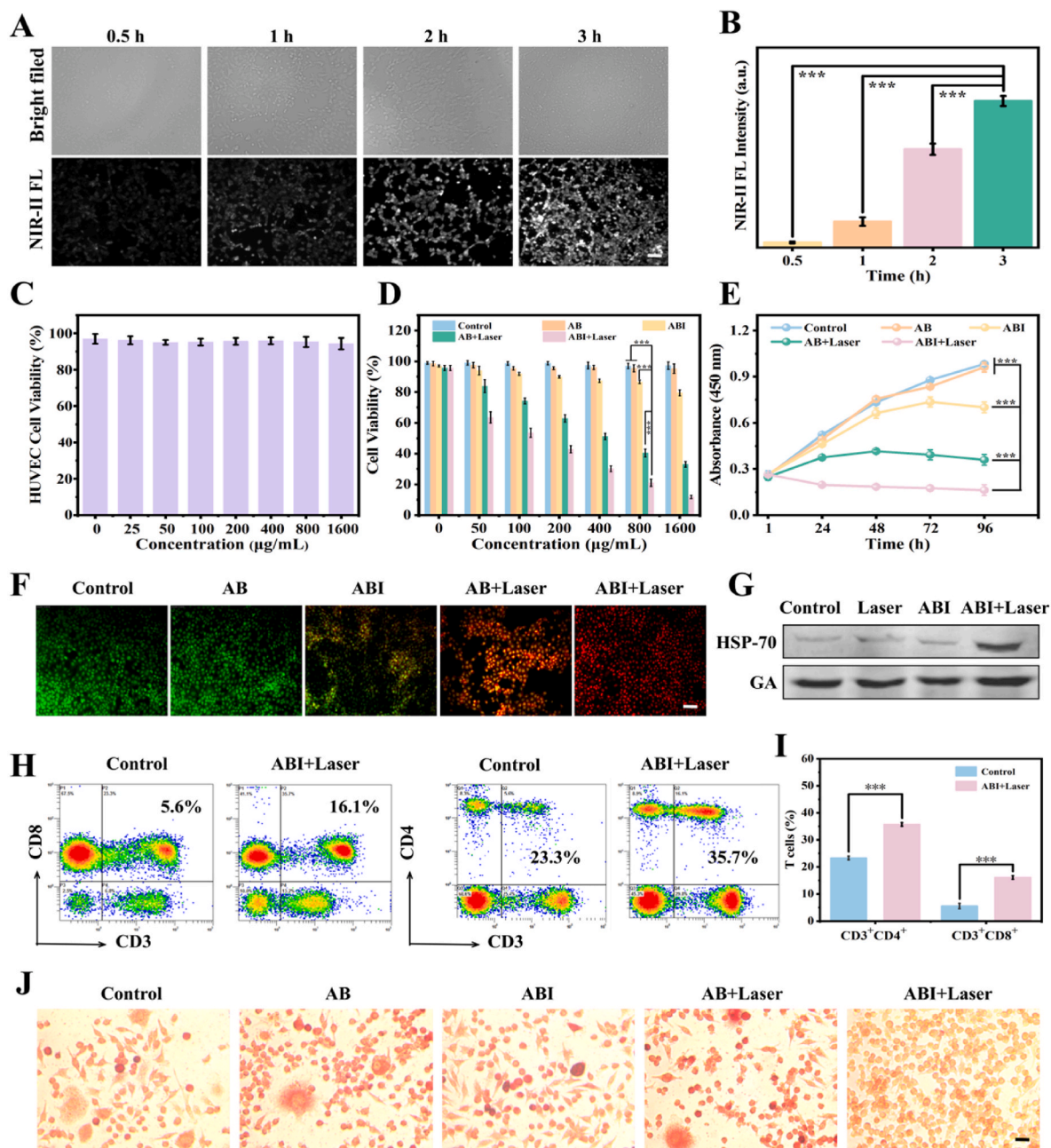
Fig. 3. A) NIR-II fluorescence images ($\lambda ex/\lambda em = 808/1000$ nm, 0.5 W, 50 ms) of 4T1 cells acquired at different time intervals (0.5, 1, 2, and 3 h) after co-culture with ABI NYs, and (B) corresponding fluorescence intensity. Scale bar: 100 μm). C) HUVEC cytotoxicity following treatment with ABI NYs at different concentrations. D) 4T1 cell viability following treatment with several groups (Control, AB, ABI, AB + Laser, ABI + Laser). E) 4T1 cells growth curves were analyzed at 800 μg/mL for several groups. The morphological study of F) cell apoptosis using AO/EB staining. G) Western blot study of HSP70 in 4T1 cells treated with various treatments. H) Flow cytometry quantifications and (I) corresponding percentages of $CD4^+$ and $CD8^+$ T cells (gated on $CD3^+$) from bone tumors. J) Representative images of tartrate-resistant acid phosphatase (TRAP)-stained cells (scale bar: 100 μm). All data are expressed as mean ± S. D (n = 5), *P < 0.05, **P < 0.01; ***P < 0.001.

negligible cytotoxicity of ABI NYs was observed in HUVEC normal cells even at concentrations up to 1600 μg/mL, thereby demonstrating the good biocompatibility of ABI NYs for biomedical applications. In addition, with an additional 808 nm laser irradiation, the toxicity of ABI NYs was increased drastically in a significant concentration-dependent manner (Fig. 3D). Concurrently, the proliferation of 4T1 cells was explored at 800 μg/mL every 24 h under different treatments. As shown in Fig. 3E, the proliferation of 4T1 cells treated with ABI + Laser demonstrated the greatest resistance, which may be mainly attributed to the superior photothermal performance. Furthermore, the living/dead cell assays of 4T1 cells were conducted by the dual acridine orange-ethidium bromide (AO/EB) staining. A majority of dead 4T1 cells are observed when treated with ABI + Laser, exhibiting significant cell apoptosis compared with the other groups, which was similar to the

CCK-8 results (Fig. 3F). Noteworthy, the colony efficiency assay further demonstrated that the ABI + Laser significantly suppressed the proliferation ability and reduced colony-forming potential (Fig. S9), which confirmed a superior therapeutic efficacy of ABI + Laser group compared to the other groups (Fig. S10). Typically, mammalian cells contain HSP70, whose functions in immune response have been extensively studied [33,34]. HSP70 is essential for capturing antigens and antigen presentation and is closely linked to the ability of cells to withstand heat. Therefore, we measured their dynamic changes in 4T1 cells during the different treatment using western blot. As observed in Fig. 3G, compared with PBS group, the expression levels of HSP70 almost no change after treating with either ABI or Laser group. Whereas the expression of HSP70 significantly upregulated under the co-treatment of ABI + Laser group, proving that thermal stress
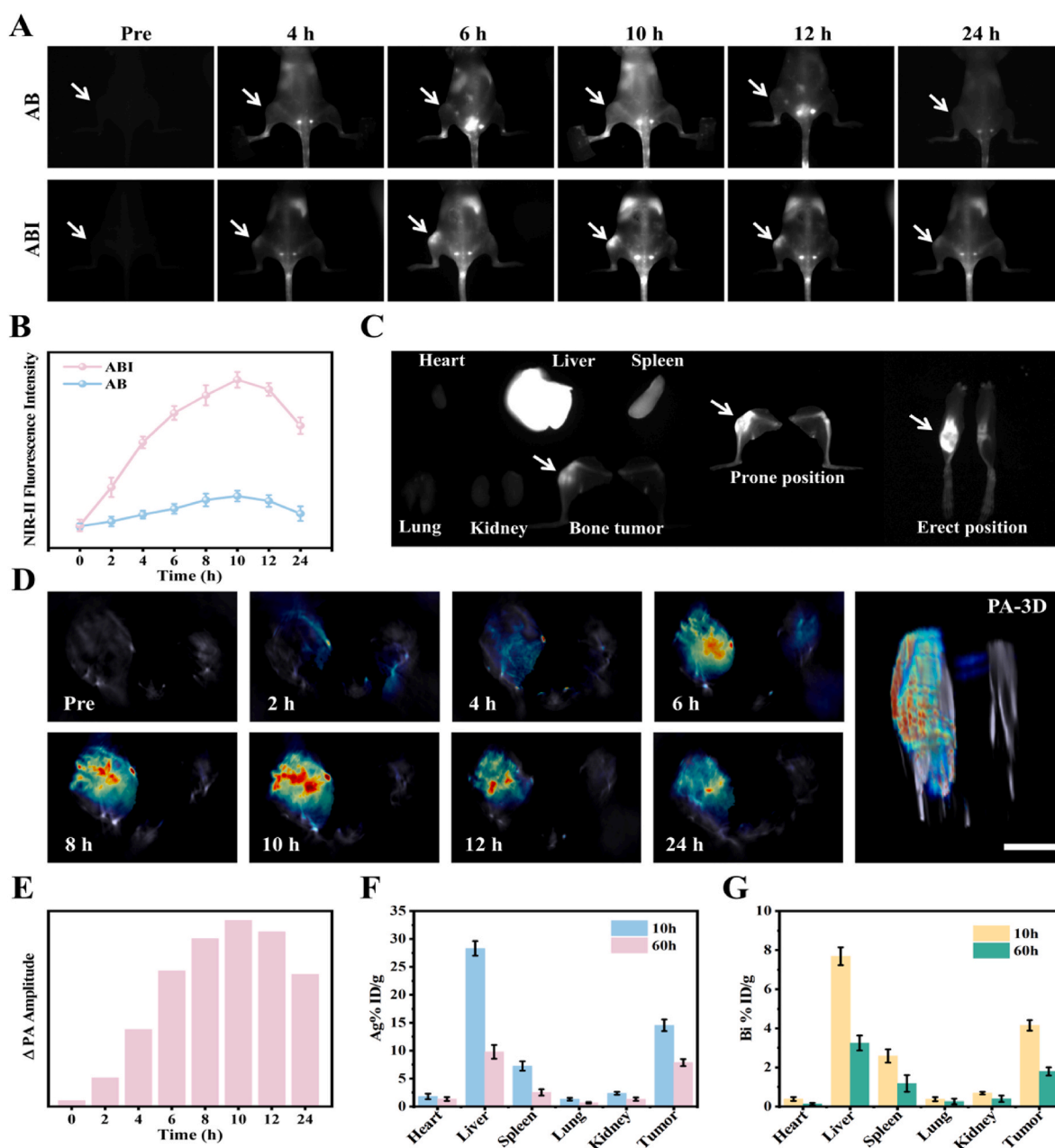
Fig. 4. A) Time-related NIR-II FL imaging after ABI NYs intravenous injection in model mice with bone metastases. B) The corresponding fluorescence changes determined by NIR-II FL imaging. C) *Ex vivo* NIR II FL imaging of dissected bone metastatic tumor and organs. D) PA imaging of bone metastatic model mice after intravenous administration of ABI NYs at different time points. Scale bar: 10 mm. E) Quantitative analysis of PA images measured from (D). Distribution of Ag (F) and Bi (G) in the tissues of main organs and bone metastases.

stimulates the overexpression of HSP70. Furthermore, HSP70 has been shown to collect antigens and actively transfer them to DCs, as well as increase tumor antigen presentation, both of which are favorable for generating an antitumor immune response [35,36]. In order to verify the effective immune modulation, tumors and spleens infiltrated CD4$^+$ and CD8$^+$ T cells were collected and measured with flow cytometry (Fig. 3H). Following ABI-mediated photothermal-immune therapy, as seen in Fig. 3I, the percentages of both CD4$^+$ and CD8$^+$ T cells in tumors increased, suggesting a higher infiltration of activated T cells compared to other groups. Taken together, the above findings offer compelling evidence that ABI NYs showed excellent antitumor immune responses following photothermal stimulation by upregulating HSP70 [37,38]. IBN, a traditional antiosteoporosis medication, has demonstrated excellent efficacy in treating bone loss by controlling osteoclast-mediated bone resorption. To assess the activity of IBN, the osteoclastic differentiation experiments were carried out by coincubating the ABI NYs with mouse mononuclear macrophages (RAW264.7) *in vitro*. It significantly inhibited the osteoclastic differentiation of RAW264.7 cells treated with 100 ng/mL of RANKL by tartrate-resistant acid phosphatase (TRAP) stained, when ABI NYs were present (Fig. 3J). According to these data, biological activity of IBN was fully retained upon conjugation with NYs, indicating that ABI NYs has a significant deal of promise for bone-protecting *in vivo*.

To further validate the targeting ability *in vivo* and bio-distribution behaviors of ABI NYs, we employed NIR-II fluorescence and PA imaging of bone metastatic model mice, separately. As shown in Fig. 4A, the NIR-II fluorescence in bone metastatic region of the AB group gradually intensified over time during the monitoring process, owing to its excellent biocompatibility and tumor accumulation, reaching its peak at 10 h after intravenous administration. However, a weak and rapid attenuated NIR-II fluorescence signal at bone metastasis lesions was observed in the AB group, making it difficult to distinguish the tumor margin. This observation may be attributed to the limited bone-targeting capacity of it, which hinders its effectiveness in achieving a highly targeted approach for bone metastases. Remarkably, in comparison to AB, ABI NYs exhibited enhanced and expedited illumination of bone metastasis tumor sites. This superior performance can be attributed to the dual targeting mechanism, which not only facilitated swift and precise localization but also resulted in prolonged retention time at the tumor sites. Consequently, the post-injection fluorescence intensity of ABI NYs was observed to be 15.2 times higher than the pre-injection value, with an nearly 4.3-fold rise in comparison to the AB group (Fig. 4B). The findings suggest that ABI NYs exhibit significant potential in enhancing the targeting efficacy of bone metastases and enabling precise localization imaging of such metastases. At 24 h post-injection, *ex vivo* NIR-II fluorescence images of anatomical tumors and major organs were obtained from each group to further assess the biodistribution characteristics of ABI NYs (Fig. 4C). Encouragingly, the ABI NYs group demonstrated a significantly enhanced NIR-II fluorescence intensity specifically in the tumor sites compared to other organs, indicating a robust enrichment performance of ABI NYs in targeting bone metastases. The fluorescence results further confirmed that ABI NYs were mostly found in the liver, spleen, and bone metastases, providing additional evidence for their ability to precise target bone metastases.

The precise targeting of tumors is imperative for the efficacy of cancer treatment. In addition to demonstrating exceptional tumor enrichment in NIR-II fluorescence imaging, the ABI NYs performed exceptionally well in PA imaging, allowing for accurate dual-modality tumor identification. Through the recording of PA signals at different times within the tumor, the PA imaging characteristics of ABI NYs were further assessed in mice used as models for bone metastases. The PA signal at the bone metastases exhibited a gradually increased over time, as depicted in Fig. 4D, and reached its peak at 10 h. Furthermore, 3D-PA imaging revealed that ABI NYs were preferentially accumulated in the bone marrow cavity and metastatic sites, indicating the dual targeting

and accumulation of ABI NYs within the tumor. The above results were further confirmed by semi-quantitative analysis of PA imaging (Fig. 4E). Based on the aforementioned analysis, 10 h after injection was shown to be the ideal irradiation period for photothermal treatment.

To comprehensively quantitatively measure the biodistribution and tumor accumulation of ABI NYs, we subsequently analyzed the Ag and Bi contents in tumors and major organs at predefined time intervals (10 and 60 h) post-injection via ICP. After 10 h following injection, the retention rates of Ag and Bi within bone metastases were recorded as 13.75% and 4.22%, respectively (Fig. 4F and G). It is noteworthy that the concentrations of Ag and Bi rapidly decreased in 60 h, which suggests efficient metabolism of ABI NYs in all tissues. Accordingly, ABI NYs can serve as a NIR-II/PA imaging contrast agent for dual-mode accurate imaging of bone metastases, thereby providing valuable insights for precise treatment.

Motivated by the exciting efficacy of treatment *in vitro*, we next assessed the phototheranostic ability of ABI NYs after successfully establishing the breast cancer bone metastasis model (Fig. 5A). Ten hours after injection, real-time temperature changes in mice were recorded with an infrared thermal imaging camera. As shown in Fig. 5B, the tumor temperature of the ABI + Laser group clearly rose by 23.8 °C within 5 min after 808 nm laser treatment. This was judged adequate to induce optimal PTT. For the PBS + Laser group, however, there was a hardly noticeable rise in temperature. These results validated the photothermal effectiveness of ABI NYs *in vivo* when exposed to the 808 nm laser. Then, throughout the duration of the therapy, the tumor volume was observed every two days to examine the tumor suppressants effectiveness of ABI NYs. Four groups were randomly selected from among the bone metastasis-bearing mice with tumor sizes less than 100 mm^3: (1) Control, (2) ABI, (3) AB + Laser, and (4) ABI + Laser. Fig. 5C shows that the tumors in three control groups grew rapidly, indicating that just the laser irradiation or ABI alone had a little impact on the tumor growth. In addition, we employed X-ray to monitor bone destruction. As expected, a substantial inhibition of tumor growth was found in the ABI + Laser group. With the prolongation of the treatment cycle, the Control group experienced unregulated tumor proliferation, resulting in painful swelling and shortening deformities. Meanwhile, a worm-like erosion edges with severe bone destruction was observed in the modeling area (Fig. 5D). Whereas the ABI group showed some degree of tumor suppression in the initial stages of treatment, but the tumors still caused severe bone destruction in the late stages. The intervention of laser exposure delayed the progression of the bone metastatic lesions, with limited erosion of the tibia. This remarkable effect may be attributed to the modification of IBN facilitated active targeting of NYs, leading to enhanced tumor suppression. As seen in Fig. 5E, the tumors expanded quickly in the three control groups, indicating that the laser irradiation or ABI alone had little influence on the tumor growth. Nevertheless, the tumor in ABI + Laser group development may be successfully suppressed or perhaps completely eliminated, demonstrating the better *in vivo* therapeutic efficacy of ABI NYs. As a consequence, the ABI + Laser group experienced the optimal percent survival rate (60 %) at 50 days post-treatment (Fig. 5G). Furthermore, no significant body weight loss was detected in all these four groups (Fig. 5F), displaying the good biocompatibility of ABI NYs.

On the basis of the preceding analysis, we further investigated osteoclast formation and assessed its functional state. TRAP is one of biomarkers in bone tissue reflecting bone resorption and osteoclasts *in vivo*. Tumor-loaded proximal tibiae were stained with TRAP immunohistochemically (IH) to identify alterations of the bone microenvironment in the growth plate region. As shown in Fig. 6A, numerous TRAP-positive areas were observed along the growth plate region in the Control group. The interaction between osteoclasts and cancer cells may be responsible for this phenomena, since it creates a "vicious cycle" that encourages osteolysis and tumor growth. The expression of TRAP was significantly reduced after ABI + Laser treatment, in comparison to the other control groups. After 16 days of treatment, three-dimensional
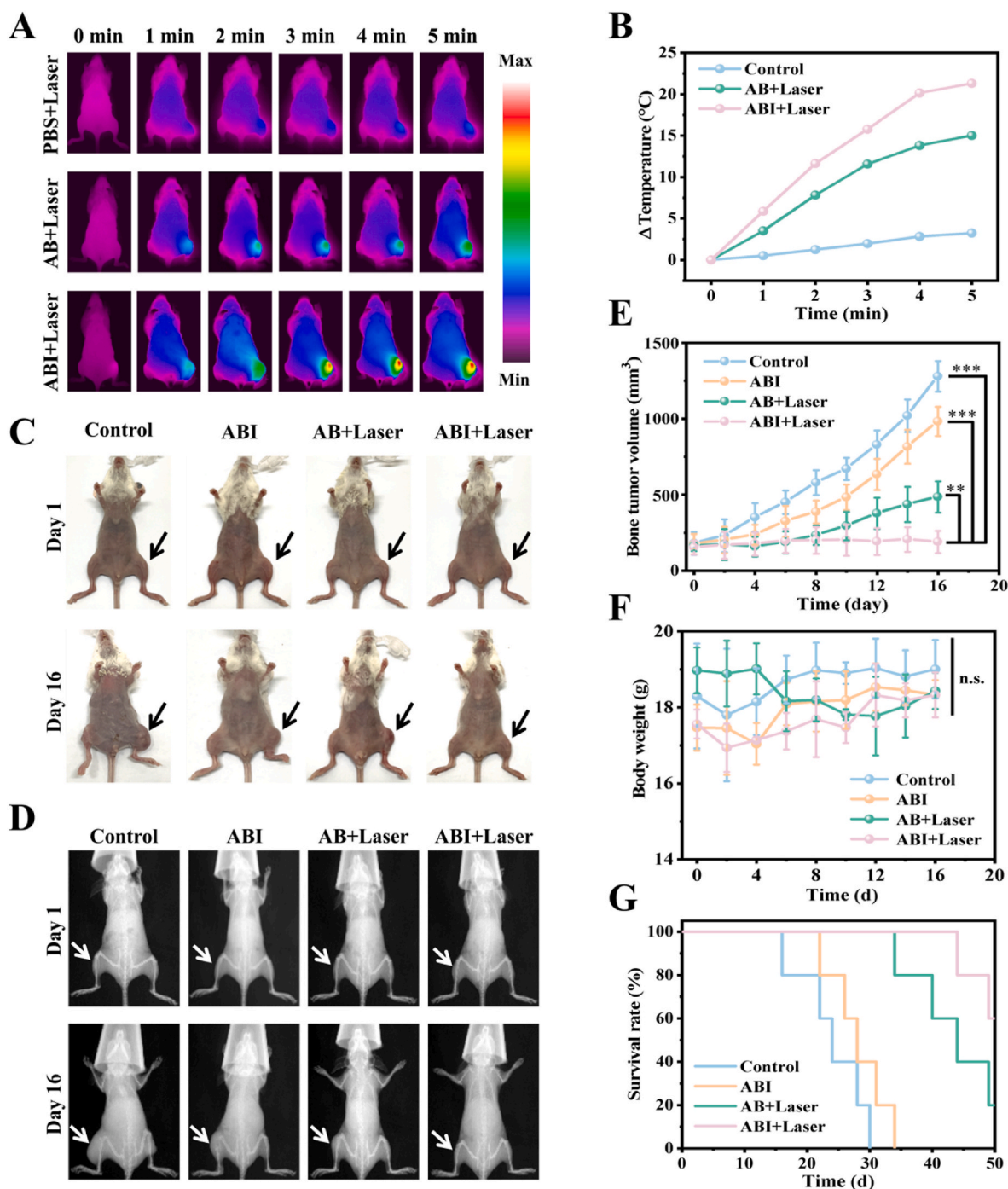
Fig. 5. A) Infrared thermal images. B) The corresponding bone metastatic lesions temperature curves of PBS, AB, and ABI NYs under 808 nm laser irradiation (1 W/cm^2, 5 min). C) Representative photographs and D) X-ray images in various groups (Control, ABI, AB + Laser, and ABI + Laser). E) Variations in tumor volume across several groups throughout therapy. F) The body weight changes of the indicated different groups after treatments over 16 days. G) Survival rates of bone metastatic model mice with various treatments. All data are expressed as mean ± S. D (n = 5), *P < 0.05, **P < 0.01; ***P < 0.001.

reconstruction images of mouse tibia were analyzed by Micro-CT scanning. As shown in Fig. 6B, the control group showed marked osteolysis, expansive bone destruction, cortical discontinuity, marginal bone sclerosis, and ossification. It is worth noting that the group receiving ABI + Laser treatment had significant tumor inhibition, clear boundaries of the bone tissue of the tumor-bearing limb, and intact bone cortex. The AB + Laser group did not achieve a comparable level of inhibition to the ABI + Laser group, although it exhibited a milder degree of bone destruction. Comparing the ABI + Laser group to the other Control groups, quantitative analysis showed substantial increases in bone metrics, such as

increased bone volume (Fig. 6C), increased bone mineral content (Fig. 6D), and higher bone mineral density (Fig. 6E). To further investigate the bone protective ability of ABI NYs, tibial sections were stained with hematoxylin-eosin (H&E) and Masson's trichrome. H&E staining of the control group showed cortical bone erosion, decreased number of bone trabeculae, increased osteolysis area, and loss of normal structural units in bone tissue (Fig. 6F). In ABI + Laser group, the cortical bone thickening and trabecular bone area increased. Similar results were observed with Masson's trichrome staining. (Fig. 6G).

To evaluate the safety of intravenous administration of ABI NYs, a
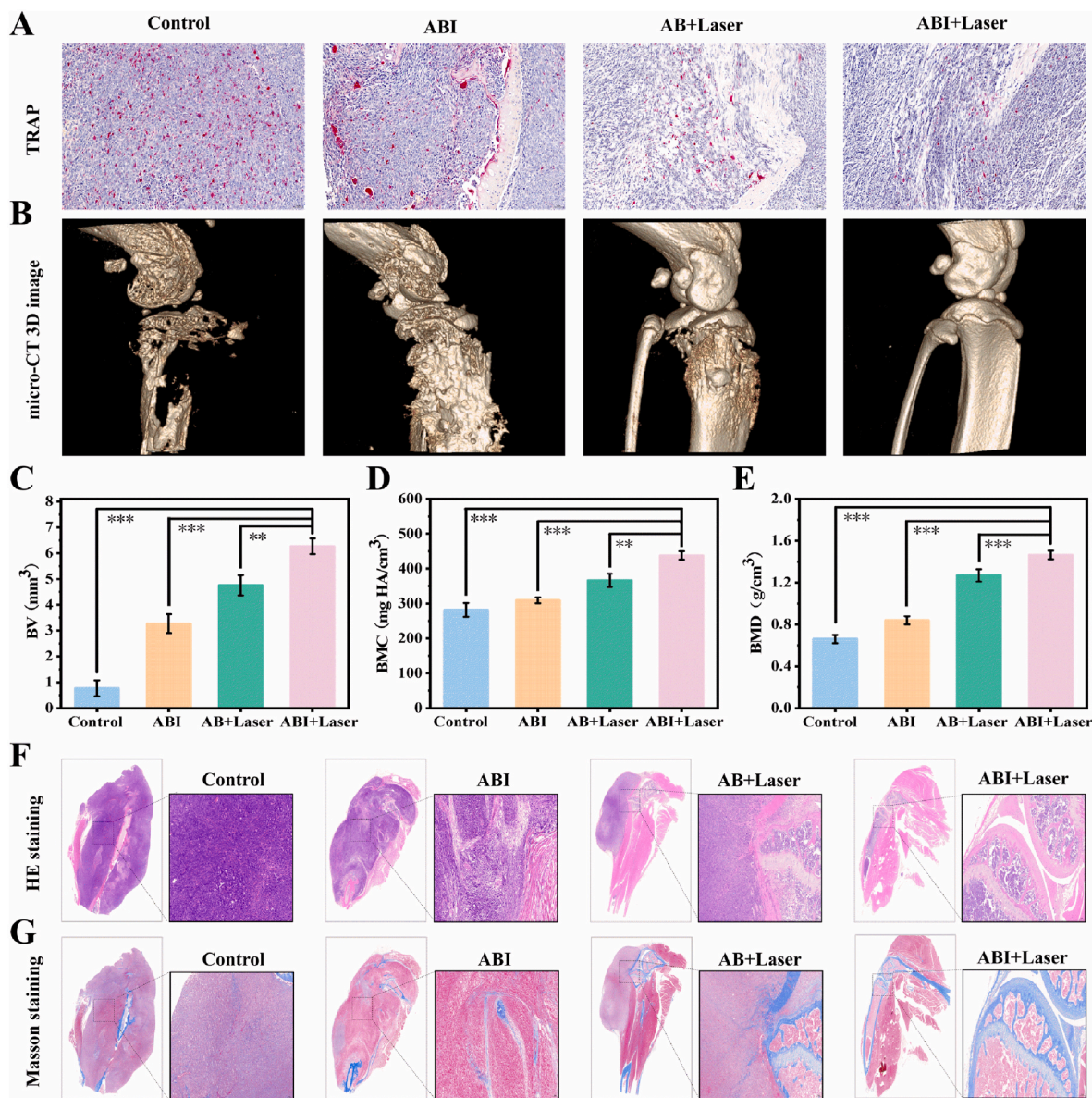
Fig. 6. A) TRAP staining of bone tumor tissue. B) Micro-CT images of metastatic tumor tibia after treatment. C-E) Quantitative analysis of Micro-CT data: bone volume (BV), bone mineral content (BMC) and bone mineral density (BMD) respectively. Histological assessment of the bone tissue decalcified sections stained with HE F) and Masson G). All data are expressed as mean ± S. D (n = 5), *P < 0.05, **P < 0.01; ***P < 0.001.

hemolysis experiment was first conducted. The results, revealing no discernible swelling, rupture, or coagulation of red blood cells after 3 h, confirmed its good biocompatibility *in vitro* (Fig. S11). After more analysis of the blood biochemistry, it was discovered that there were no appreciable differences between the groups in the standard biochemical (ALT, AST, CREA, BUN) and hematological (RBC, WBC, PLT, Gran) characteristics. (Fig. S12). In the meanwhile, H&E staining was used to assess the histopathological alterations in the primary organs (heart, liver, spleen, lung, and kidney), and the results showed natural tissue shape with no changes (Fig. S13). When considered collectively, these findings showed that ABI NYs had high *in vivo* biocompatibility for possible clinical theranostic applications.

3. Conclusion

In this study, we developed an original all-in-one nanosystem for early detection and effective therapy of bone metastases, combining anti-tumor and bone-repair therapeutic properties with NIR-II FL/PA

dual-modal imaging in a single component. The ABI NYs targetted microscopic lesions of bone metastasis through an active and passive dual-targeting strategy. Excitingly, *in vivo* results demonstrated that ABI NYs could precisely localize metastasis lesions with NIR-II FL and PA imaging. Furthermore, the combination of ABI NYs and NIR not only activate photothermal effect to ablate the early metastases lesions, but also suppress the tumor growth and early osteolysis by improving the bone microenvironment. Significantly, photothermal effectt was applied to induce the upregulation of HSP70, further provoke immunogenic cell death (ICD) effect and anti-tumor immune response. Overall, *in vitro* and *in vivo* tests, the "one-component, multi-functions" technique demonstrated good anti-tumor and bone repair performance, which emphasizing the benefits of ABI NYs for early theranostics of bone metastases.

Experimental section

Methods and any associated references are available in the Supporting Information.

CRediT authorship contribution statement

Xin Zhang: Writing – original draft, Validation, Data curation, Conceptualization. **Wenxuan Wang:** Investigation, Formal analysis, Data curation. **Xiaochun Zheng:** Investigation, Formal analysis, Data curation. **Chongqing Zhang:** Methodology, Investigation, Data curation. **Yarong Jin:** Investigation, Formal analysis, Data curation. **Shichao Meng:** Visualization, Software, Methodology. **Jinxuan Li:** Visualization, Software, Methodology. **Rong Dai:** Visualization, Software, Methodology. **Weiwei Kang:** Software, Methodology, Investigation. **Ziliang Zheng:** Writing – review & editing, Investigation, Funding acquisition, Conceptualization. **Ruiping Zhang:** Supervision, Project administration, Funding acquisition.

Declaration of competing interest

The authors declare that they have no known competing financial interests or personal relationships that could have appeared to influence the work reported in this paper.

Data availability

The authors do not have permission to share data.

Appendix A. Supplementary data

Supplementary data to this article can be found online at https://doi.org/10.1016/j.mtbio.2024.101052.

References

[1] L. Zhang, J. Qu, Y. Qi, Y. Duan, Y.-W. Huang, Z. Zhou, P. Li, J. Yao, B. Huang, S. Zhang, D. Yu, Nat. Commun. 13 (2022) 2543.
[2] J.J. Yin, C.B. Pollock, K. Kelly, Cell Res. 15 (2005) 57.
[3] Y. Liang, H. Zhang, X. Song, Q. Yang, Semin. Cancer Biol. 60 (2020) 14.
[4] Z. Song, J. Miao, M. Miao, B. Cheng, S. Li, Y. Liu, Q. Miao, Q. Li, M. Gao, Adv. Sci. 10 (2023) e2300217.
[5] F. Salvador, A. Llorente, R.R. Gomis, J. Pathol. 249 (2019) 6.
[6] J. Zarrer, M.-T. Haider, D.J. Smit, H. Taipaleenmäki, Biomolecules 10 (2020) 337.
[7] C. Li, G. Jiang, J. Yu, W. Ji, L. Liu, P. Zhang, J. Du, C. Zhan, J. Wang, B.Z. Tang, Adv. Mater. 35 (2023) e2208229.
[8] J. Huang, C. Zhang, X. Wang, X. Wei, K. Pu, Angew. Chem., Int. Ed. Engl. 62 (2023) e202303982.
[9] P. Sun, F. Qu, C. Zhang, P. Cheng, X. Li, Q. Shen, D. Li, Q. Fan, Adv. Sci. 9 (2022) e2204718.
[10] J.C. Li, K.Y. Pu, Chem. Soc. Rev. 48 (2019) 38.
[11] S. Yoon, M. Kim, M. Jang, Y.W. Choi, W.J. Choi, S.S. Kang, W.S. Choi, Nat. Rev. Phys. 2 (2020) 141.
[12] P. Pei, Y. Chen, C.X. Sun, Y. Fan, Y.M. Yang, X. Liu, L.F. Lu, M.Y. Zhao, H.X. Zhang, D.Y. Zhao, X.G. Liu, F. Zhang, Nat. Nanotechnol. 16 (2021) 1011.
[13] Y. Kenry, K. Duan, B. Liu, Adv. Mater. 30 (2018) 1802394.
[14] A.B.E. Attia, G. Balasundaram, M. Moothanchery, U.S. Dinish, R. Bi, V. Ntziachristos, M. Olivo, Photoacoustics 16 (2019) 100144.
[15] Q.S. Zhang, P. Yu, Y. Fan, C.X. Sun, H.S. He, X. Liu, L.F. Lu, M.Y. Zhao, H.X. Zhang, F. Zhang, Angew. Chem., Int. Ed. 133 (2021) 4013.
[16] Q. Wang, Y. Dai, J. Xu, J. Cai, X. Niu, L. Zhang, R. Chen, Q. Shen, W. Huang, Q. Fan, Adv. Funct. Mater. 29 (2019) 1901480.
[17] S. Thangudu, N. Kaur, C. Korupalli, V. Sharma, P. Kalluru, R. Vankayala, Biomater. Sci. 9 (2021) 5472.
[18] X.Q. Li, Y.C. Pan, C. Chen, Y.F. Gao, X.L. Liu, K.Y. Yang, X.W. Luan, D.T. Zhou, F. Zeng, X. Han, Y.J. Song, Angew. Chem., Int. Ed. 133 (2021) 21370.
[19] N. Dai, Z.Q. Sun, H.H. Zhao, D.S. Qi, X.Y. Li, D.Y. Gao, M.X. Li, Q.L. Fan, Q. M. Shen, W. Huang, Biomaterials 275 (2021) 120935.
[20] X. Fu, Y. Huang, H. Zhao, E. Zhang, Q. Shen, Y. Di, F. Lv, L. Liu, S. Wang, Adv. Mater. 33 (2021) e2102570.
[21] Y. Gao, Q. Zhao, M. Xiao, X. Huang, X. Wu, Biomaterials 273 (2021) 120792.
[22] Q. Chen, C. Wang, Z. Zhan, W. He, Z. Cheng, Y. Li, Z. Liu, Biomaterials 35 (2014) 8206.
[23] S.M. Hashemi, Z.M. Hassan, S. Soudi, T. Ghazanfari, M. Kheirandish, S. Shahabi, Int. Immunopharm. 7 (2007) 920.
[24] X. Fu, Y. Huang, H. Zhao, E. Zhang, Q. Shen, Y. Di, F. Lv, L. Liu, S. Wang, Adv. Mater. 33 (2021) e2102570.
[25] X. Li, S. He, B. Luo, P. Li, X. Chen, M. Wu, C. Song, C. Liu, T. Yang, X. Zhang, X. Yang, J. Hu, Small 19 (2023) e2303541.
[26] T. Shang, X. Yu, S. Han, B. Yang, Biomater. Sci. 8 (2020) 5241.
[27] H. He, Y. Lin, Z.-Q. Tian, D.-L. Zhu, Z.-L. Zhang, D.-W. Pang, Small 14 (2018) e1703296.
[28] Y. Wang, Y.Y. Wu, Y.J. Liu, J. Shen, L. Lv, L.B. Li, L.C. Yang, J.F. Zeng, Y.Y. Wang, L.S.W. Zhang, Z. Li, M.Y. Gao, Z.F. Chai, Adv. Funct. Mater. 26 (2016) 5335–5344.
[29] D.-H. Zhao, X.-Q. Yang, X.-L. Hou, Y. Xuan, X.-L. Song, Y.-D. Zhao, W. Chen, Q. Wang, B. Liu, J. Mater. Chem. B 7 (2019) 2484.
[30] J. Zhong, Q. Zhang, Z. Zhang, K. Shi, Y.C. Sun, T. Liu, J. Lin, Nano Res. 15 (2022) 153–161.
[31] W. Sun, K. Ge, Y. Jin, Y. Han, H. Zhang, G. Zhou, X. Yang, D. Liu, H. Liu, X.-J. Liang, J. Zhang, ACS Nano 13 (2019) 7556.
[32] M. Chang, Z. Hou, M. Wang, C. Yang, R. Wang, F. Li, D. Liu, T. Peng, C. Li, J. Lin, Angew. Chem. Int. Ed. 60 (2021) 12971.
[33] Z. Li, X. Lai, S. Fu, L. Ren, H. Cai, H. Zhang, Z. Gu, X. Ma, K. Luo, Adv. Sci. 9 (2022) e2201734.
[34] R. Guo, S. Wang, L. Zhao, Q. Zong, T. Li, G. Ling, P. Zhang, Biomaterials 282 (2022) 121425.
[35] P.A. MacAry, B. Javid, R.A. Floto, K.G. Smith, W. Oehlmann, M. Singh, P.J. Lehner, Immunity 20 (2004) 95.
[36] D. Arnold, S. Faath, H. Rammensee, H. Schild, J. Exp. Med. 182 (1995) 885.
[37] M.H. Moehler, M. Zeidler, V. Wilsberg, J.J. Cornelis, T. Woelfel, J. Rommelaere, P. R. Galle, M. Heike, Hum. Gene Ther. 16 (2005) 996.
[38] T. Chen, J. Guo, C. Han, M. Yang, X. Cao, J. Immunol. 182 (2009) 1449.